

Titanium-Based Nanoscale Metal-Organic Framework for Type I Photodynamic Therapy

Guangxu Lan, Kaiyuan Ni, Samuel S. Veroneau, Xuanyu Feng,
Geoffrey T Nash, Taokun Luo, Ziwan Xu, and Wenbin Lin

J. Am. Chem. Soc., **Just Accepted Manuscript** • DOI: 10.1021/jacs.8b13804 • Publication Date (Web): 19 Feb 2019

Downloaded from <http://pubs.acs.org> on February 19, 2019

Just Accepted

“Just Accepted” manuscripts have been peer-reviewed and accepted for publication. They are posted online prior to technical editing, formatting for publication and author proofing. The American Chemical Society provides “Just Accepted” as a service to the research community to expedite the dissemination of scientific material as soon as possible after acceptance. “Just Accepted” manuscripts appear in full in PDF format accompanied by an HTML abstract. “Just Accepted” manuscripts have been fully peer reviewed, but should not be considered the official version of record. They are citable by the Digital Object Identifier (DOI®). “Just Accepted” is an optional service offered to authors. Therefore, the “Just Accepted” Web site may not include all articles that will be published in the journal. After a manuscript is technically edited and formatted, it will be removed from the “Just Accepted” Web site and published as an ASAP article. Note that technical editing may introduce minor changes to the manuscript text and/or graphics which could affect content, and all legal disclaimers and ethical guidelines that apply to the journal pertain. ACS cannot be held responsible for errors or consequences arising from the use of information contained in these “Just Accepted” manuscripts.

Titanium-Based Nanoscale Metal-Organic Framework for Type I Photodynamic Therapy

Guangxu Lan,^{‡,1} Kaiyuan Ni,^{‡,1} Samuel S. Veroneau,¹ Xuanyu Feng,¹ Geoffrey T. Nash,¹ Taokun Luo,¹ Ziwang Xu,¹ and Wenbin Lin^{*,1,2}

¹Department of Chemistry and ²Department of Radiation and Cellular Oncology and Ludwig Center for Metastasis Research, The University of Chicago, Chicago, IL 60637, USA.

Supporting Information Placeholder

ABSTRACT: Nanoscale metal-organic frameworks (nMOFs) have shown great potential as nanophotosensitizers for photodynamic therapy (PDT) owing to their high photosensitizer loadings, facile diffusion of reactive oxygen species (ROSs) through their porous structures, and intrinsic biodegradability. The exploration of nMOFs in PDT, however, remains limited to an oxygen-dependent type II mechanism. Here we report the design of a new nMOF, Ti-TBP, composed of Ti-oxo chain second building units (SBUs) and photosensitizing 5,10,15,20-tetra(*p*-benzoato)porphyrin (TBP) ligands, for hypoxia-tolerant type I PDT. Upon light irradiation, Ti-TBP not only sensitizes singlet oxygen production, but also transfers electrons from excited TBP* species to Ti⁴⁺-based SBUs to afford TBP^{•+} ligands and Ti³⁺ centers, thus propagating the generation of superoxide, hydrogen peroxide, and hydroxyl radicals. By generating four distinct ROSs, Ti-TBP-mediated PDT elicits superb anticancer efficacy with >98% tumor regression and 60% cure rate.

With structural regularity and tunability, high porosity, and intrinsic biodegradability, nanoscale metal-organic frameworks (nMOFs) hold great potential in biomedical applications¹⁻⁹ such as photodynamic therapy (PDT).¹⁰⁻¹⁶ In PDT, the structural and compositional tunability of nMOFs allows the incorporation of a variety of photosensitizers (PSs) to afford high PS loadings, while the structural regularity of nMOFs keeps PSs isolated from each other to avoid self-quenching. The high porosity of nMOFs facilitates the diffusion of reactive oxygen species (ROSs) to exert cytotoxic effects whereas the biodegradability of nMOFs alleviates the concern of long-term toxicity.

Although PDT is an efficient anti-cancer treatment,¹⁷⁻²⁰ it largely relies upon an oxygen-dependent type II mechanism through energy transfer from excited PSs to molecular oxygen (O₂) to generate singlet oxygen (¹O₂).²¹ Therapeutic efficacy of type II PDT is diminished in hypoxic environments found in many solid tumors.²² In contrast, type I PDT is more hypoxia-tolerant by generating cytotoxic radicals via electron transfer (ET) from excited PSs to O₂ and organic molecules.²³⁻²⁵ We hypothesized that the tunability of nMOFs can be harnessed to enable type I PDT. Herein, we report the synthesis of a novel nMOF, Ti-TBP, and its use in the first type I PDT mediated by nMOFs (Figure 1). In addition to sensitizing ¹O₂ generation, Ti-TBP produces superoxide (O₂^{•-}), hydrogen peroxide (H₂O₂), and hydroxyl radicals (•OH) via transferring electrons from excited TBP* species to Ti⁴⁺-based SBUs to form TBP^{•+} ligands and Ti³⁺ centers. The generation of

four distinct ROSs leads to superb anticancer efficacy with >98% tumor regression and 60% cure rate.

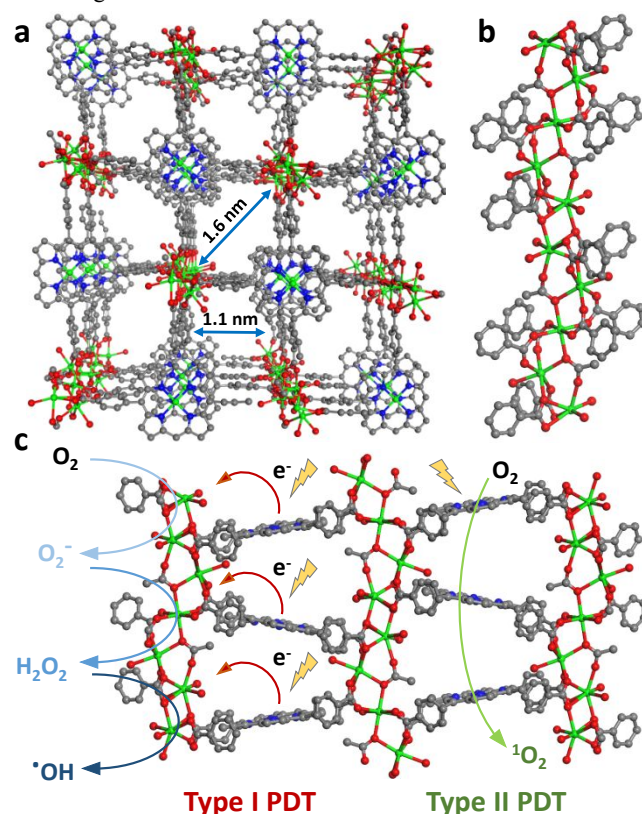


Figure 1. (a) Perspective view of Ti-(Ti-TBP) structure along the (010) direction. (b) Coordination environments of Ti-oxo chain SBUs. (c) Schematic showing both type I and type II PDT enabled by Ti-TBP.

Violet square-shaped crystals of Ti-(Ti-TBP) were synthesized through a solvothermal reaction between TiCl₄·2THF and 5,10,15,20-tetra(*p*-benzoato)porphyrin (H₄TBP) in *N,N*-dimethylformamide with acetic acid (AcOH) as the modulator at 120 °C for 7 days. Single crystal X-ray diffraction studies revealed that the TBP ligands were metalated with Ti during crystal growth and the Ti-coordinated TBP (Ti-TBP) ligands were linked by infinite Ti-oxo chain SBUs to form a 3D framework of the new topology with a point symbol of {4¹⁸.6²².8⁴.10}{4².6}{4⁶.6⁹}{4} (Figure 1a and S2-3, SI). Each repeat unit of the Ti-oxo chain has

five Ti^{4+} ions that are bridged by carboxylate groups from TBP or acetate ligands and terminated by hydroxide groups (Figure 2a and S1, SI). Negligible Cl was detected in Ti-(Ti-TBP) by X-ray fluorescence (Cl:Ti = 0.0016:1), leading to a formula of $[\text{Ti}_5(\text{Ti-TBP})_2(\text{OAc})_2(\text{OH})_6](\text{OAc})_8$.

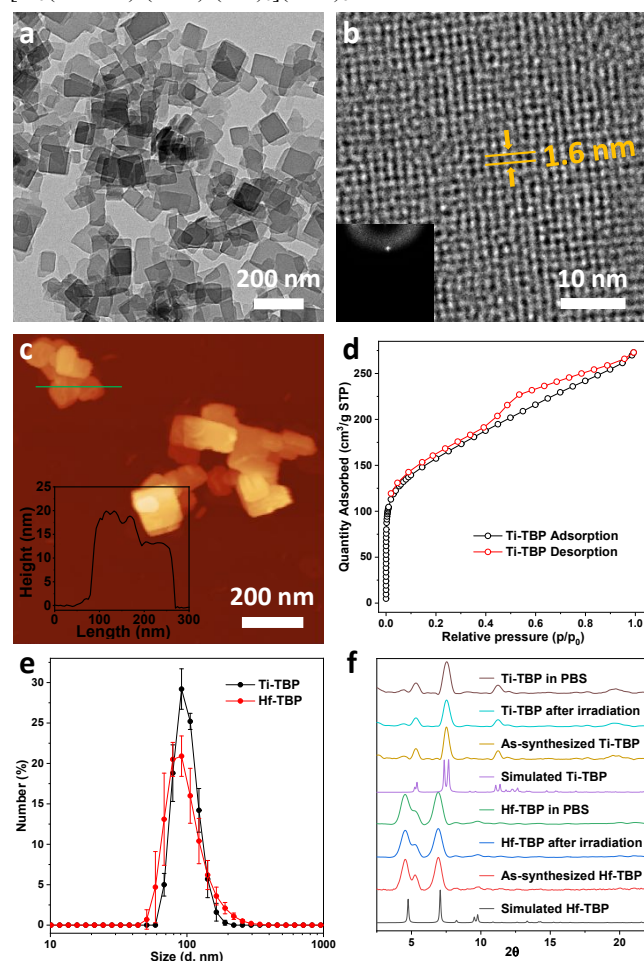


Figure 2. TEM image (a), HRTEM image and FFT pattern (inset) (b), AFM topography and height profile (inset) (c), and nitrogen sorption isotherms (d) of Ti-TBP nMOFs. Number-averaged diameters in water (e). PXRD patterns of Ti-TBP and Hf-TBP after light irradiation for 15 min or soaking in 0.6 mM phosphate saline buffer for 8 h (f).

Lowering the reaction temperature to 80 °C led to the synthesis of Ti-TBP nMOF with non-metalated TBP ligands of the composition $[\text{Ti}_5(\text{TBP})_2(\text{OAc})_2(\text{OH})_6](\text{OAc})_4$. UV-Vis spectrum of Ti-TBP showed four characteristic Q-bands for non-metalated TBP ligands (Figure S5, SI). Thermogravimetric analysis of Ti-TBP showed a weight loss of 82.9% in the 300 to 600 °C range, matching the expected value of 82.4% (Figure S6, SI). By combining inductively coupled plasma-mass spectrometry (ICP-MS) analysis of Ti and UV-Vis analysis of TBP in digested Ti-TBP, we determined the Ti:TBP ratio as 2.67 ± 0.16 , which is close to 2.5 expected for Ti-TBP but much lower than 3.5 expected for Ti-(Ti-TBP).

Transmission electron microscope (TEM) imaging of Ti-TBP revealed square nanoplates with a diameter of ~150 nm (Figure 2a) while atomic force microscopy (AFM) topography of Ti-TBP gave a plate thickness of ~20 nm (Figure 2c and S4, SI). Dynamic light scattering (DLS) measurements gave a diameter of 100.1 ± 4.0 nm for Ti-TBP (Figure 2e). The porous structure of Ti-TBP was confirmed by nitrogen sorption isotherms at 77 K with a Brunauer-Emmett-Teller (BET) surface area of 527.7 m²/g (Figure 2d). High

resolution TEM (HRTEM) imaging and fast Fourier transform (FFT) patterns of Ti-TBP revealed a 4-fold symmetry, consistent with the Ti-TBP structure projected in the (010) direction (Figure 2b). The distance between two adjacent lattice points in HRTEM was measured to be ~1.6 nm, matching the distance between the centers of two adjacent Ti-chain SBUs. Moreover, powder X-ray diffraction (PXRD) pattern of Ti-TBP matched well with that simulated from its idealized structure (Figure 2f).

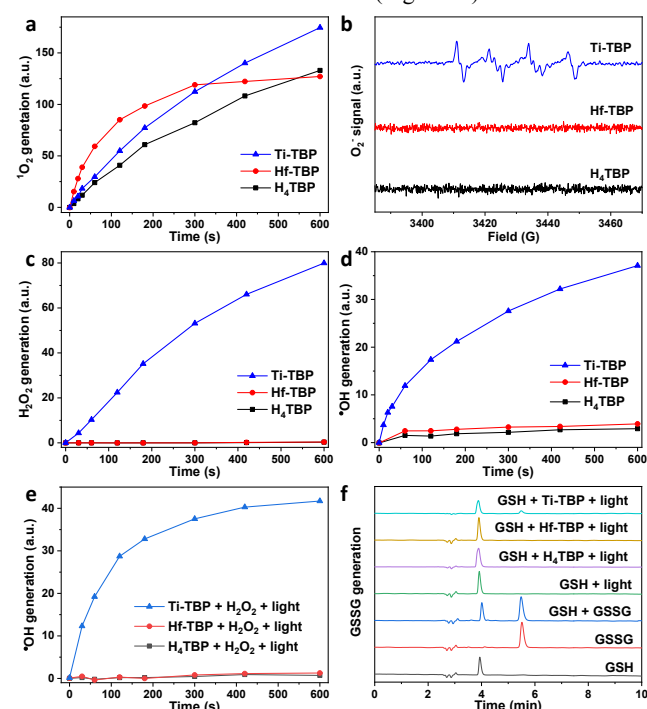


Figure 3. Time-dependent ¹O₂ generation (a), O₂⁻ generation (b), and time-dependent H₂O₂ generation (c) and ·OH generation (d) upon light irradiation under oxygenated conditions. Time-dependent enhanced ·OH generation from H₂O₂ (e) and GSSG generation from GSH (f) upon light irradiation under oxygen-free conditions.

We hypothesized that upon light irradiation, Ti^{4+} centers in Ti-TBP SBUs could be reduced to Ti^{3+} centers ($\text{Ti}^{4+} \rightarrow \text{Ti}^{3+}$, $E = -0.50$ V vs. NHE)²⁶ via ET from the photo-excited TBP* to form TBP^{•+}, in addition to energy transfer from TBP* to O₂ to generate ¹O₂ (type II PDT). The generated Ti^{3+} further reduces O₂ to generate O₂⁻, H₂O₂, and ·OH to enable type I PDT (Figure 1c). The Hf-TBP nMOF based on redox-inert Hf₆ SBUs ($\text{Hf}^{4+} \rightarrow \text{Hf}^{3+}$, $E = -1.55$ V vs. NHE)²⁷ was used as a control. PXRD, TEM, and DLS measurements showed that crystalline Hf-TBP exhibited a diameter of 100.0 ± 8.3 nm (Figure 1e, 1f, and S7, SI). Upon light irradiation, Ti-TBP, Hf-TBP, and H₄TBP effected Type II PDT via ¹O₂ generation as determined by singlet oxygen sensor green (SOSG) assays (Figure 3a). Only Ti-TBP enabled type I PDT by generating a series of distinct ROSS, including O₂⁻ as determined by electron paramagnetic resonance (EPR) with 5-tert-butoxycarbonyl-5-methyl-1-pyrroline-N-oxide (BMPO) as a spin trap (Figure 3b), H₂O₂ as determined with a hydrogen peroxide assay kit (Figure 3c), and ·OH as determined by aminophenyl fluorescein (APF) assay (Figure 3d).

To demonstrate that Ti-TBP-enabled type I PDT can tolerate hypoxia of solid tumors, we mimicked hypoxic cancer cell environments with an oxygen-free aqueous solution containing either H₂O₂ (in high concentration in hypoxic cancer cells)²² or glutathione (GSH, a ubiquitous antioxidant in cells).²⁸ Upon light irradiation, Ti-TBP effectively reduced H₂O₂ through Ti^{3+} to generate highly cytotoxic ·OH, while Hf-TBP and H₄TBP or Ti-

TBP without light irradiation did not enhance $\cdot\text{OH}$ generation (Figure 3e and S8, SI). Furthermore, TBP^{2+} elicited oxidative stress by oxidizing GSH to glutathione disulfide (GSSG) as determined by high performance liquid chromatograph (Figure 3f and S9, SI).

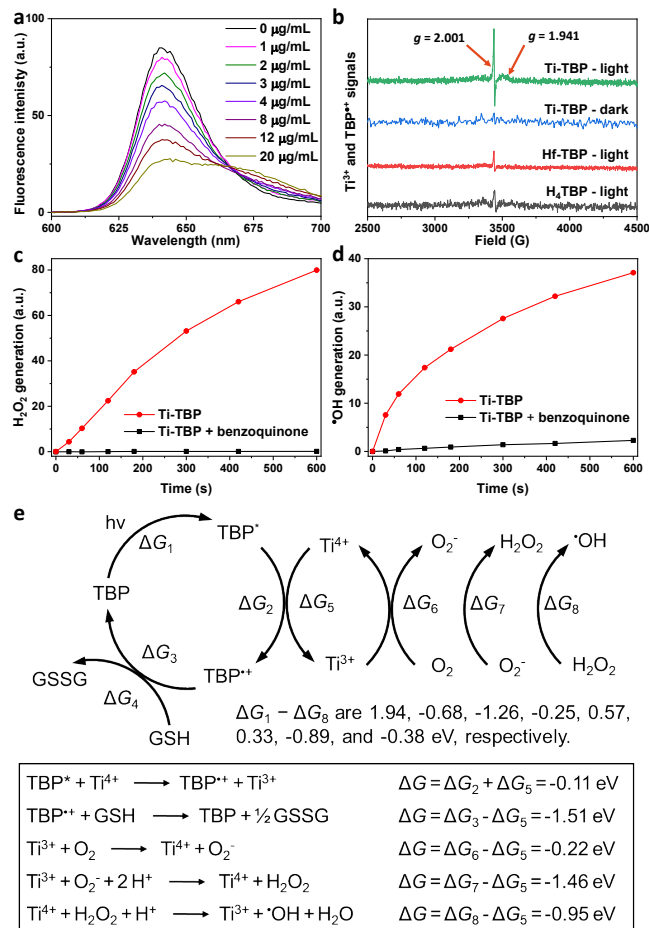


Figure 4. (a) Emission spectra of 20 μM H_4TBP with addition of different amounts of $\text{TiCl}_4 \cdot 2\text{THF}$. (b) EPR spectra showed the generation of Ti^{3+} ($g = 1.941$) and TBP^{2+} ($g = 2.001$) upon light irradiation at 20 K. Time-dependent H_2O_2 (c) and $\cdot\text{OH}$ (d) generation by Ti-TBP with or without benzoquinone upon light irradiation. (e) Proposed mechanism for Ti-TBP enabled type I PDT at pH 7.

The mechanism of Ti-TBP-enabled type I PDT was next investigated. H_4TBP luminescence was quenched by $\text{TiCl}_4 \cdot 2\text{THF}$ with a Stern-Völmer constant (K_{SV}) of $36.05 \pm 0.67 \text{ mM}^{-1}$, suggesting efficient ET from TBP^* to Ti^{4+} (Figure 4a and S10, SI). Consistent with this, TBP luminescence was totally quenched in Ti-TBP (Figure S11, SI). EPR spectra of Ti-TBP upon light irradiation showed a sharp peak with a g -value of 2.001 that is attributable to TBP^{2+} and a weak broad peak with a g -value of 1.941 that is assignable to Ti^{3+} species (Figure 4b).³⁰ No EPR signals were observed for Ti-TBP in dark, and only faint EPR signals corresponding to TBP^{2+} were observed in Hf-TBP and H_4TBP upon light irradiation. The EPR results thus directly prove ET in Ti-TBP. To understand Ti^{3+} -mediated ROS generation, O_2^- was scavenged by benzoquinone to evaluate its influence on other ROSs (Figure S12, SI).³¹ $^1\text{O}_2$ generation of Ti-TBP decreased at the same proportion as the emission of H_4TBP (Figure S13 and S14, SI) due to luminescence quenching by benzoquinone. Negligible amounts of H_2O_2 and $\cdot\text{OH}$ were detected in the presence of benzoquinone (Figure 3c-d), demonstrating that both H_2O_2 and $\cdot\text{OH}$ are generated from O_2^- . We have thus shown that Ti^{3+} can propagate the generation of O_2^- , H_2O_2 , and $\cdot\text{OH}$ under light irradiation.

We propose the mechanism of Ti-TBP enabled type I PDT in Figure 4e and Section S4.4 (SI). Photoexcitation of TBP to TBP^* (ΔG_1 , calculated from the emission peak of H_4TBP at 641 nm) generates Ti^{3+} and TBP^{2+} via ET. The Ti^{3+} centers generate O_2^- , H_2O_2 , and $\cdot\text{OH}$ whereas TBP^{2+} oxidizes GSH to GSSG (Figure 4e). The energy difference between TBP^* to TBP^{2+} ($\Delta G_2 = -\Delta G_1 - \Delta G_3$) is enough to drive the reduction of Ti^{4+} to Ti^{3+} (ΔG_5 , determined by the CV of $\text{TiCl}_4 \cdot 2\text{THF}$). The Ti^{3+} centers sequentially reduce O_2 to generate O_2^- (ΔG_6), H_2O_2 (ΔG_7), and $\cdot\text{OH}$ (ΔG_8).³² The oxidation potential of TBP^{2+} to TBP (ΔG_3), determined by cyclic voltammogram (CV) of H_4TBP , is sufficient to oxidize GSH to GSSG (ΔG_4).

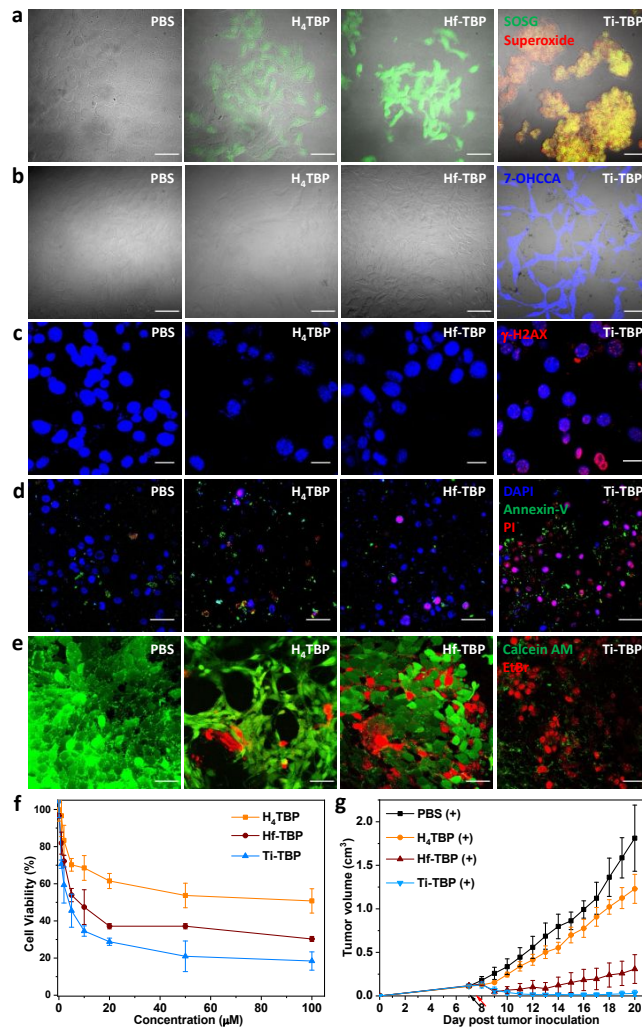


Figure 5. (a) Detection of $^1\text{O}_2$ (green) and O_2^- (red) generation by SOSG and a superoxide kit. Green and red fluorescence merged as yellow fluorescence. (b) Coumarin-3-carboxylic acid assay showed $\cdot\text{OH}$ generation via fluorescence of generated 7-OH coumarin-3-carboxylic acid (blue). (c) $\gamma\text{-H}_2\text{AX}$ assays showed DNA DSBs. Scale bar = 20 μm . (d) Annexin-V assay probed apoptotic cell death process. DAPI (blue), FITC-Annexin-V (green) and PI (red) indicate nucleus, apoptotic and dead cells, respectively. (e) Live and dead cell assay demonstrated cell killing effect. Calcein AM (green) and Ethidium Bromide (EtBr, red) dye indicate live and dead cell, respectively. Scale bar = 50 μm except in (c). (f) MTS assay showed anti-cancer effect in CT26 cells. (g) In vivo anti-cancer effect on CT26 tumor-bearing BALB/c mice. N = 5. Black and red arrows refer to intratumoral injection and light irradiation, respectively.

The cytotoxicity of Ti-TBP-mediated PDT was investigated in vitro in CT26 cells. ICP-MS analysis demonstrated efficient uptake

of Ti-TBP and Hf-TBP by CT26 cells (Figure S17, SI). Although H₄TBP, Hf-TBP, and Ti-TBP can all generate ¹O₂, O₂^{•-} was only detected in cells treated with Ti-TBP (Figure 5a and S18, SI). The in vitro generation of [•]OH was verified by direct [•]OH detection via coumarin-3-carboxylic acid assay (Figure 5b and S19, SI) and by DNA double strand break (DSB) quantification with γ -H2AX assay (Figure 5c and S20, SI), both of which showed that [•]OH was only detected in Ti-TBP treated cells. Confocal imaging and flow cytometry using an Annexin V/dead cell apoptosis kit showed that significant numbers of cells underwent apoptosis when treated with Ti-TBP (Figure 5d and S21-22, SI). MTS assay and live/dead cell confocal microscopic images showed that Ti-TBP outperformed Hf-TBP with IC₅₀ values of 3.4 ± 0.7 and 7.8 ± 2.4 μ M, respectively (Figure 5e-f, and S23-24, SI).

The therapeutic effects of Ti-TBP-mediated PDT were next evaluated in vivo on a colorectal adenocarcinoma model of CT26-tumor bearing BALB/c mice. When the tumors reached 100-150 mm³, Ti-TBP, Hf-TBP, H₄TBP or PBS was injected intratumorally at a TBP doses of 0.2 μ mol following by light irradiation (650 nm, 180 J/cm²). Ti-TBP treatment led to effective tumor regression of 98.4% in volume with a cure rate of 60% (3 out of 5), when compared to that of the PBS dark control on Day 20. Hf-TBP and H₄TBP treatment showed moderate and slight tumor inhibition, respectively (Figure 5g). The averaged weights of excised tumors on Day 20 treated with Ti-TBP, Hf-TBP, H₄TBP or PBS were 0.027 ± 0.037 g, 0.127 ± 0.03 g, 0.617 ± 0.168 g, or 1.734 ± 0.291 g, respectively (Figure S26-27, SI). H&E staining indicated severe necrosis of tumor slices from Ti-TBP treatment (Figure S28, SI). Steady body weights, similar weight gain patterns, and no difference in behaviors and organ functions were observed in all groups, indicating lack of systemic toxicity for Ti-TBP treatment (Figure S25, SI). The lack of abnormalities on histological images of frozen major organ slices further supported the non-toxic nature of Ti-TBP-mediated PDT treatment (Figure S29, SI).

In summary, we report the synthesis of Ti-TBP and its use in hypoxia-tolerant type I PDT with superb anti-cancer efficacy. Upon light irradiation, the proximity of Ti-oxo chain SBUs to TBP ligands (~1.1 nm) facilitates ET to generate TBP^{•+} and Ti³⁺, propagating the generation of O₂^{•-}, H₂O₂, and [•]OH. Our work uncovers a new strategy to implement and understand type I PDT using nMOFs.

ASSOCIATED CONTENT

Supporting Information

The Supporting Information is available free of charge on the ACS Publications website.

Synthesis and characterization of Ti-(Ti-TBP) and Ti-TBP, ROS generation, mechanistic studies, and anti-cancer efficacy (PDF)

Data for Ti-(Ti-TBP) (CIF)

AUTHOR INFORMATION

Corresponding Author

wenbinlin@uchicago.edu

Author Contributions

‡These authors contributed equally.

Notes

The authors declare no competing financial interests.

ACKNOWLEDGMENT

We thank Dr. Alexander Filatov for help with single crystal refinement, Vlad Kamysbayev for help with X-ray fluorescence, and Zhe Li for help with CV study. We acknowledge the National Cancer Institute (U01-CA198989 and 1R01CA216436) and the University of Chicago Medicine Comprehensive Cancer Center (NIH CCSG: P30 CA014599) for funding support. Single crystal diffraction studies were performed at ChemMatCARS, APS, ANL. NSF's ChemMatCARS Sector 15 is principally supported by the Divisions of Chemistry (CHE) and Materials Research (DMR), National Science Foundation, under grant number NSF/CHE-1346572. Use of the Advanced Photon Source, an Office of Science User Facility operated for the U.S. Department of Energy (DOE) Office of Science by Argonne National Laboratory, was supported by the U.S. DOE under Contract No. DE-AC02-06CH11357.

REFERENCES

1. Furukawa, H.; Cordova, K. E.; O'Keeffe, M.; Yaghi, O. M., The Chemistry and Applications of Metal-Organic Frameworks. *Science* **2013**, *341* (6149), 1230444.
2. Lu, K.; He, C.; Guo, N.; Chan, C.; Ni, K.; Lan, G.; Tang, H.; Pelizzari, C.; Fu, Y.-X.; Spiotto, M. T.; Weichselbaum, R. R.; Lin, W., Low-dose X-ray radiotherapy–radiodynamic therapy via nanoscale metal–organic frameworks enhances checkpoint blockade immunotherapy. *Nat. Biomed. Eng.* **2018**, *2* (8), 600-610.
3. Ni, K.; Lan, G.; Chan, C.; Quigley, B.; Lu, K.; Aung, T.; Guo, N.; La Riviere, P.; Weichselbaum, R. R.; Lin, W., Nanoscale metal-organic frameworks enhance radiotherapy to potentiate checkpoint blockade immunotherapy. *Nat. Commun.* **2018**, *9* (1), 2351.
4. Rabone, J.; Yue, Y. F.; Chong, S. Y.; Stylianou, K. C.; Bacsá, J.; Bradshaw, D.; Darling, G. R.; Berry, N. G.; Khimyak, Y. Z.; Ganin, A. Y.; Wiper, P.; Claridge, J. B.; Rosseinsky, M. J., An Adaptable Peptide-Based Porous Material. *Science* **2010**, *329* (5995), 1053.
5. Morris, W.; Briley, W. E.; Auyeung, E.; Cabezas, M. D.; Mirkin, C. A., Nucleic Acid–Metal Organic Framework (MOF) Nanoparticle Conjugates. *J. Am. Chem. Soc.* **2014**, *136* (20), 7261-7264.
6. Levine, D. J.; Runčevski, T.; Kapelewski, M. T.; Keitz, B. K.; Oktawiec, J.; Reed, D. A.; Mason, J. A.; Jiang, H. Z. H.; Colwell, K. A.; Legendre, C. M.; FitzGerald, S. A.; Long, J. R., Olsalazine-Based Metal–Organic Frameworks as Biocompatible Platforms for H₂ Adsorption and Drug Delivery. *J. Am. Chem. Soc.* **2016**, *138* (32), 10143-10150.
7. Cui, Y.; Yue, Y.; Qian, G.; Chen, B., Luminescent Functional Metal–Organic Frameworks. *Chem. Rev.* **2012**, *112* (2), 1126-1162.
8. Wu, P.; Wang, J.; He, C.; Zhang, X.; Wang, Y.; Liu, T.; Duan, C., Luminescent Metal–Organic Frameworks for Selectively Sensing Nitric Oxide in an Aqueous Solution and in Living Cells. *Adv. Funct. Mater.* **2012**, *22* (8), 1698-1703.
9. Foucault-Collet, A.; Gogick, K. A.; White, K. A.; Villette, S.; Pallier, A.; Collet, G.; Kieda, C.; Li, T.; Geib, S. J.; Rosi, N. L.; Petoud, S., Lanthanide near infrared imaging in living cells with Yb³⁺ nano metal organic frameworks. *Proc. Natl. Acad. Sci.* **2013**, 201305910.
10. Lan, G.; Ni, K.; Lin, W., Nanoscale metal–organic frameworks for phototherapy of cancer. *Coord. Chem. Rev.* **2019**, *379*, 65-81.
11. Lan, G.; Ni, K.; Xu, Z.; Veroneau, S. S.; Song, Y.; Lin, W., Nanoscale Metal–Organic Framework Overcomes Hypoxia for Photodynamic Therapy Primed Cancer Immunotherapy. *J. Am. Chem. Soc.* **2018**, *140* (17), 5670-5673.
12. Zeng, J.-Y.; Zou, M.-Z.; Zhang, M.; Wang, X.-S.; Zeng, X.; Cong, H.; Zhang, X.-Z., π -Extended Benzoporphyrin-Based Metal–Organic Framework for Inhibition of Tumor Metastasis. *ACS Nano* **2018**, *12* (5), 4630-4640.
13. Zheng, X.; Wang, L.; Pei, Q.; He, S.; Liu, S.; Xie, Z., Metal–Organic Framework@Porous Organic Polymer Nanocomposite for Photodynamic Therapy. *Chem. Mater.* **2017**, *29* (5), 2374-2381.
14. Park, J.; Jiang, Q.; Feng, D.; Mao, L.; Zhou, H.-C., Size-Controlled Synthesis of Porphyrinic Metal–Organic Framework and Functionalization for Targeted Photodynamic Therapy. *J. Am. Chem. Soc.* **2016**, *138* (10), 3518-3525.
15. Lismont, M.; Dreesen, L.; Wuttke, S., Metal-Organic Framework Nanoparticles in Photodynamic Therapy: Current Status and Perspectives. *Adv. Funct. Mater.* **2017**, *27* (14), 1606314.
16. Lu, K.; He, C.; Lin, W., Nanoscale Metal–Organic Framework

for Highly Effective Photodynamic Therapy of Resistant Head and Neck Cancer. *J. Am. Chem. Soc.* **2014**, *136* (48), 16712-16715.

17. Spring, B. Q.; Bryan Sears, R.; Zheng, L. Z.; Mai, Z.; Watanabe, R.; Sherwood, M. E.; Schoenfeld, D. A.; Pogue, B. W.; Pereira, S. P.; Villa, E.; Hasan, T., A photoactivable multi-inhibitor nanoliposome for tumour control and simultaneous inhibition of treatment escape pathways. *Nat. Nanotech.* **2016**, *11*, 378.

18. Lovell, J. F.; Jin, C. S.; Huynh, E.; Jin, H.; Kim, C.; Rubinstein, J. L.; Chan, W. C. W.; Cao, W.; Wang, L. V.; Zheng, G., Porphyrin nanovesicles generated by porphyrin bilayers for use as multimodal biophotonic contrast agents. *Nat. Mater.* **2011**, *10*, 324.

19. Huang, P.; Lin, J.; Wang, X.; Wang, Z.; Zhang, C.; He, M.; Wang, K.; Chen, F.; Li, Z.; Shen, G.; Cui, D.; Chen, X., Light-Triggered Theranostics Based on Photosensitizer-Conjugated Carbon Dots for Simultaneous Enhanced-Fluorescence Imaging and Photodynamic Therapy. *Adv. Mater.* **2012**, *24* (37), 5104-5110.

20. Zhang, Y.; Jeon, M.; Rich, L. J.; Hong, H.; Geng, J.; Zhang, Y.; Shi, S.; Barnhart, T. E.; Alexandridis, P.; Huizinga, J. D.; Seshadri, M.; Cai, W.; Kim, C.; Lovell, J. F., Non-invasive multimodal functional imaging of the intestine with frozen micellar naphthalocyanines. *Nat. Nanotech.* **2014**, *9*, 631.

21. Dolmans, D. E. J. G. J.; Fukumura, D.; Jain, R. K., Photodynamic therapy for cancer. *Nat. Rev. Cancer* **2003**, *3*, 380.

22. Kim, J.; Cho, H. R.; Jeon, H.; Kim, D.; Song, C.; Lee, N.; Choi, S. H.; Hyeon, T., Continuous O₂-Evolving MnFe₂O₄ Nanoparticle-Anchored Mesoporous Silica Nanoparticles for Efficient Photodynamic Therapy in Hypoxic Cancer. *J. Am. Chem. Soc.* **2017**, *139* (32), 10992-10995.

23. Gilson, R. C.; Black, K. C. L.; Lane, D. D.; Achilefu, S., Hybrid TiO₂-Ruthenium Nano-photosensitizer Synergistically Produces Reactive Oxygen Species in both Hypoxic and Normoxic Conditions. *Angew. Chem. Int. Ed.* **2017**, *56* (36), 10717-10720.

24. Vakrat-Haglili, Y.; Weiner, L.; Brumfeld, V.; Brandis, A.; Salomon, Y.; McLlroy, B.; Wilson, B. C.; Pawlak, A.; Rozanowska, M.; Sarna, T.; Scherz, A., The Microenvironment Effect on the Generation of Reactive Oxygen Species by Pd-Bacteriopheophorbide. *J. Am. Chem. Soc.* **2005**, *127* (17), 6487-6497.

25. Castano, A. P.; Demidova, T. N.; Hamblin, M. R., Mechanisms in photodynamic therapy: part one—photosensitizers, photochemistry and cellular localization. *Photodiagnosis and Photodynamic Therapy* **2004**, *1* (4), 279-293.

26. Guang-sen, C.; Okido, M.; Oki, T., Electrochemical studies of titanium ions (Ti⁴⁺) in equimolar KCl NaCl molten salts with 1 wt% K₂TiF₆. *Electrochim. Acta* **1987**, *32* (11), 1637-1642.

27. Lu, K.; He, C.; Guo, N.; Chan, C.; Ni, K.; Weichselbaum, R. R.; Lin, W., Chlorin-Based Nanoscale Metal-Organic Framework Systemically Rejects Colorectal Cancers via Synergistic Photodynamic Therapy and Checkpoint Blockade Immunotherapy. *J. Am. Chem. Soc.* **2016**, *138* (38), 12502-12510.

28. Trachootham, D.; Alexandre, J.; Huang, P., Targeting cancer cells by ROS-mediated mechanisms: a radical therapeutic approach? *Nat. Rev. Drug Discov.* **2009**, *8*, 579.

29. Lan, M.; Zhao, H.; Yuan, H.; Jiang, C.; Zuo, S.; Jiang, Y., Absorption and EPR spectra of some porphyrins and metalloporphyrins. *Dyes Pigm.* **2007**, *74* (2), 357-362.

30. Ji, P.; Song, Y.; Drake, T.; Veroneau, S. S.; Lin, Z.; Pan, X.; Lin, W., Titanium(III)-Oxo Clusters in a Metal-Organic Framework Support Single-Site Co(II)-Hydride Catalysts for Arene Hydrogenation. *J. Am. Chem. Soc.* **2018**, *140* (1), 433-440.

31. Samoilova, R. I.; Crofts, A. R.; Dikanov, S. A., Reaction of Superoxide Radical with Quinone Molecules. *J. Phys. Chem. A* **2011**, *115* (42), 11589-11593.

32. Wood, P. M., The potential diagram for oxygen at pH 7. *Biochem. J* **1988**, *253* (1), 287.

TOC:

